

# Local Atomic and Electronic Structure of Boron Chemical Doping in Monolayer Graphene

Liuyan Zhao,<sup>†</sup> Mark Levendorf,<sup>‡</sup> Scott Goncher,<sup>§</sup> Theanne Schiros,<sup>||</sup> Lucia Pálová,<sup>§</sup> Amir Zabet-Khosousi,<sup>§</sup> Kwang Taeg Rim,<sup>§</sup> Christopher Gutiérrez,<sup>†</sup> Dennis Nordlund,<sup>⊥</sup> Cherno Jaye,<sup>¶</sup> Mark Hybertsen,<sup>□</sup> David Reichman,<sup>§</sup> George W. Flynn,<sup>§</sup> Jiwoong Park,<sup>‡</sup> and Abhay N. Pasupathy<sup>\*†</sup>

<sup>†</sup>Department of Physics, Columbia University, New York, New York 10027, United States

<sup>‡</sup>Chemistry Department, Cornell University, Ithaca, New York 10065, United States

<sup>§</sup>Chemistry Department and <sup>||</sup>Energy Frontier Research Center, Columbia University, New York, New York 10027, United States

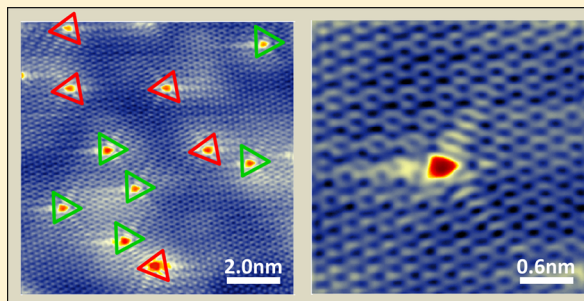
<sup>⊥</sup>Stanford Synchrotron Radiation Lightsource, SLAC National Accelerator Laboratory, Menlo Park, California 94025, United States

<sup>¶</sup>Materials Measurement Laboratory, National Institute of Standards and Technology, Gaithersburg, Maryland 20899, United States

<sup>□</sup>Center for Functional Nanomaterials, Brookhaven National Laboratory, Upton, New York 11973, United States

## S Supporting Information

**ABSTRACT:** We use scanning tunneling microscopy and X-ray spectroscopy to characterize the atomic and electronic structure of boron-doped and nitrogen-doped graphene created by chemical vapor deposition on copper substrates. Microscopic measurements show that boron, like nitrogen, incorporates into the carbon lattice primarily in the graphitic form and contributes  $\sim 0.5$  carriers into the graphene sheet per dopant. Density functional theory calculations indicate that boron dopants interact strongly with the underlying copper substrate while nitrogen dopants do not. The local bonding differences between graphitic boron and nitrogen dopants lead to large scale differences in dopant distribution. The distribution of dopants is observed to be completely random in the case of boron, while nitrogen displays strong sublattice clustering. Structurally, nitrogen-doped graphene is relatively defect-free while boron-doped graphene films show a large number of Stone-Wales defects. These defects create local electronic resonances and cause electronic scattering, but do not electronically dope the graphene film.



**KEYWORDS:** *Graphene chemical doping, scanning tunneling microscopy/spectroscopy, boron-doped graphene, graphene functionalization, X-ray spectroscopy*

Tailoring the electronic properties of monolayer graphene can unlock many potential electronic applications of graphene.<sup>1–3</sup> In pristine undoped graphene, the Fermi level lies at the Dirac point, where the conductivity of the system reaches its minimum.<sup>1</sup> By introducing free charge carriers, the conductivity increases linearly with carrier density.<sup>4,5</sup> Tuning two regions of a single graphene sheet with electrons and holes respectively can produce p–n junctions,<sup>6,7</sup> the elementary building blocks of electronic devices. Therefore, it is crucial to control the type and concentration of charge injected into graphene, especially in the absence of external fields.

One common way to shift the chemical potential of a host material is by chemical doping with foreign atoms.<sup>8</sup> Recently, boron- (B) and nitrogen- (N) doped graphene have been produced by the inclusion of the appropriate dopant atoms during the growth of large area graphene films<sup>9–14</sup> or by suitable post treatment of existing pristine graphene layers.<sup>15–18</sup> In the case of N dopants, it is now known that the bonding environment of the dopants in the honeycomb lattice depends

on the sample preparation recipe. Both graphitic substitution (where a single N atom is  $sp^2$  bonded to three C atoms) and pyridinic N (where a N atom is bonded to less than three C atoms) can be observed in the films that are produced by chemical vapor deposition (CVD) growth on different substrates.<sup>19</sup> The two different dopant types have dramatically different effects on graphene with graphitic N dopants adding electrons to the film and pyridinic N dopants withdrawing charge.<sup>20</sup>

Unlike N-doped graphene, B-doped graphene has been much less well-explored experimentally,<sup>16,21,22</sup> and basic questions about the dopant structure, dopant distribution, and their effect on the electronic properties of graphene films remain largely unanswered. To answer these basic questions, we use atomic resolution, cryogenic scanning tunneling microscopy/spectros-

**Received:** May 15, 2013

**Revised:** September 6, 2013

**Published:** September 13, 2013



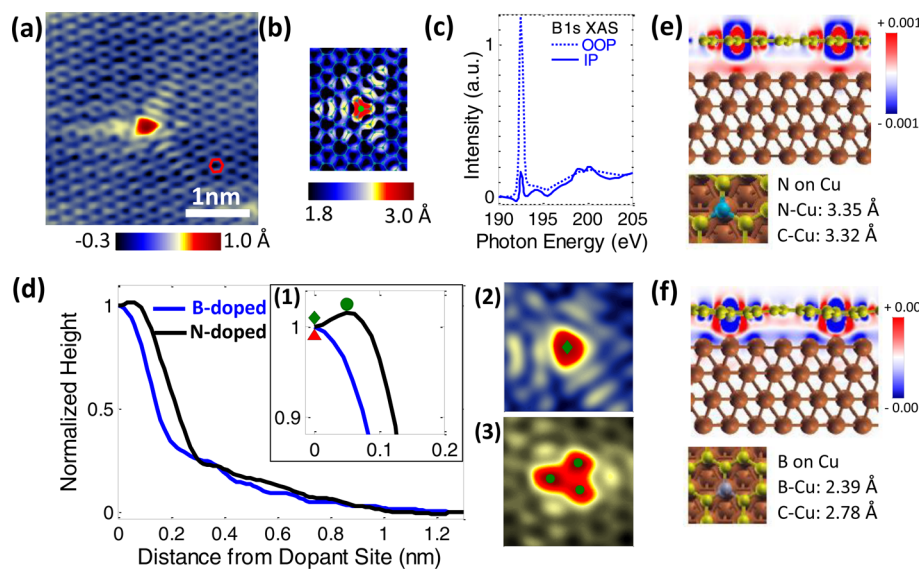


**Figure 1.** (a) STM imaging of a single graphitic boron dopant, the most common doping form observed on B-doped graphene on copper foil.  $V_{\text{bias}} = -0.5$  V and  $I_{\text{set}} = 0.5$  nA. (b) Simulated STM image of graphitic B dopant in free-standing graphene ( $V_{\text{bias}} = -0.5$  V) based on DFT calculations. Superimposed is a ball-and-stick model of the graphene lattice with a single B impurity in the center. (c) NEXAFS spectra taken on B-doped graphene with E-field polarization normal and parallel to the graphene plane. (d) Angular averaged line profile for graphitic B dopant (blue) and N dopant (black). Inset (1) Zoom of line profile shown in (d). Inset (2) and (3) High-resolution STM images of single graphitic B ( $V_{\text{bias}} = -0.5$  V and  $I_{\text{set}} = 0.5$  nA) and N ( $V_{\text{bias}} = 0.5$  V and  $I_{\text{set}} = 0.5$  nA) dopants. (e) Structure and charge density differences in N-doped graphene commensurate with Cu(111), with the N atom on top of a Cu atom. Red denotes excess charge and blue a deficit of charge. (f) Structure and charge density differences in B-doped graphene with the B atom on top of a Cu atom.

copy (STM/S) in conjunction with X-ray absorption spectroscopy to investigate the atomic and electronic structure of B-doped graphene films. The experimental results were interpreted using first principles density function theory (DFT) calculations.

B-doped graphene films were grown on polycrystalline copper foils using a mixture of  $\text{CH}_4$ ,  $\text{H}_2$ , and  $\text{B}_2\text{H}_6$  gases at 1000 °C in a quartz tube furnace.<sup>23,24</sup> Following growth, samples were transferred for STM measurements from ambient conditions into an ultrahigh-vacuum (UHV) chamber and annealed at ~350 °C for 5 h to clean the sample surface. STM/S measurements were taken at 77 K. A total of over 20 films grown using different gas flow rates and pressures were studied by STM. For comparison, we also studied N-doped graphene films grown using a mixture of  $\text{CH}_4$ ,  $\text{H}_2$ , and  $\text{NH}_3$ . In general, we found that the quality of the B-doped films was far more sensitive to the dopant gas ( $\text{B}_2\text{H}_6$ ) concentration and flow rate, when compared to N-doped graphene films. Our best B-doped films were produced by using quartz tubes that have been exposed to B before growth. In this process, the tube (with a piece of copper foil inserted) was first heated at 1000 °C at 7.0 Torr with a flow of 6 sccm of  $\text{CH}_4$  and 1–5 sccm of  $\text{B}_2\text{H}_6$  (1%  $\text{B}_2\text{H}_6$  in  $\text{H}_2$ ) for 30 min. A new piece of copper foil was then introduced into the tube and graphene growth was performed using only a mixture of 6 sccm of  $\text{CH}_4$  and 100 sccm of  $\text{H}_2$ . It is found that the prior exposure of the tube to B is sufficient to dope the graphene in subsequent growths.

A topographical scan of the best B-doped graphene samples reveal that the most common dopant feature (>80%) exhibits a triangular shaped core with three “tails” extending from the three edges of the triangle (Figure 1a). This structure exhibits all the features expected from a graphitic dopant; by following the unperturbed graphene lattice from positions far from the dopant structure (red hexagon mark in Figure 1a), we can determine that the center of the triangle is at a carbon site ( $C_B$ )

and the three apexes are at the three first neighboring carbon sites ( $C_{1B}$ ). The experimentally measured apparent dopant height is  $1.0 \pm 0.1$  Å. The experimentally measured shape of the graphitic dopant is in good agreement with DFT calculations<sup>25–28</sup> (shown in Figure 1b and discussed further below). Further confirmation that graphitic B dopants are present in the structure is provided by near edge X-ray absorption fine structure spectroscopy (NEXAFS) measurements. A NEXAFS spectrum (Figure 1c) taken on the same sample as in Figure 1a at the B edge shows clear resonances at energies of 192.0 and 200.0 eV. The intensity of the resonances is strongly dependent on the electric field polarization, and both the energy and polarization dependence of the resonances is completely consistent with the  $\pi$  and  $\sigma$  states of  $\text{sp}^2$  bonded graphitic B.<sup>16</sup>

The overall triangular symmetry of the graphitic B dopants is very similar to the case of graphitic N dopants that have been previously observed.<sup>12</sup> However, important differences exist in the details of the structure. This is best seen in the angular averaged topographic line profiles through graphitic B and N dopants, normalized to unity at the dopant sites (displayed in Figure 1d) (see Supporting Information S1 and Figure S1 for line profiles without normalization). While the topographic features for both kinds of dopants extend to a radius of about 1.0 nm, the topographic maximum occurs at different locations in the two cases. In the case of the B dopant, the maximum height is observed at the B dopant site (green diamond, inset Figure 1d). In the case of the N dopant, the maximum is observed close to the nearest carbon neighbors to the N dopant (green circle, inset Figure 1d). The difference is clearly shown in high-resolution atomic images of B and N dopants (inset 2 and 3 respectively in Figure 1d).

In a STM topographic image, an apparent height increase at a given atomic site can arise either from a real structural height increase or from electronic effects if the tunneling amplitude is

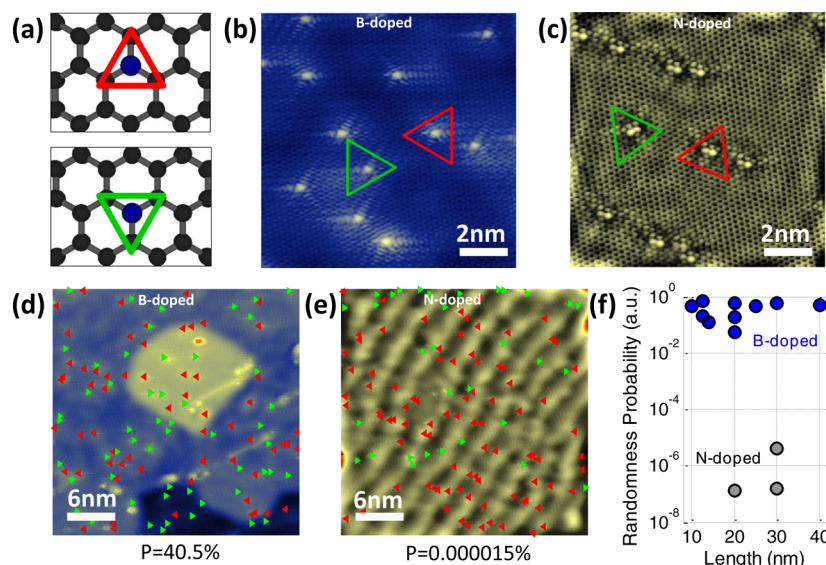


**Figure 2.** (a) Diagrams of a single graphitic B dopant in different sublattices showing the triangles formed by the three closest carbon atoms rotated by 180° with respect to each other. (b) STM image of B-doped graphene showing 5 B dopants in one sublattice and 6 in the other sublattice.  $V_{\text{bias}} = -0.5$  V and  $I_{\text{set}} = 0.5$  nA. (c) STM image of N-doped graphene with 1 N dopant in one sublattice and 10 in the other sublattice.  $V_{\text{bias}} = 0.5$  V and  $I_{\text{set}} = 0.5$  nA. (d,e) STM images of B- and N-doped graphene respectively over a large scale of  $30 \times 30$  nm<sup>2</sup>. The p-value below each image represents the probability of the dopants being distributed randomly between two sublattices. (f) p-values for 10 areas of B-doped graphene and 3 areas of N-doped graphene showing several orders of magnitude difference between B-doped and N-doped graphene.

enhanced over the atom. In order to distinguish between these two possibilities, we performed DFT calculations of the bonding environment, charge density distribution and local density of states for graphitic N- and B-doped graphene. We first performed simulations for free-standing-doped graphene layers in which the N and B dopants remain coplanar with the graphene sheet. These calculations (Figure 1b and ref 12) indicate that the apparent height difference between B and N dopants in the STM topographic images is a purely electronic effect that arises from the fact that the  $p_z$  orbital of the B dopant extends further than the  $p_z$  orbital of the N dopant.<sup>29</sup> The effect of the copper substrate was then considered by performing calculations for doped graphene on top of a commensurate slab of Cu(111) single crystal, as shown in Figure 1e,f, respectively. Our calculations show that there is a substantial difference in the interaction between the Cu substrate and the B and N dopants. The N dopants are seen to not interact significantly with Cu. They remain coplanar with the surrounding graphene with the N–C nearest neighbor distance of 1.40 Å very close to the C–C nearest neighbor distance of 1.41 Å. Similarly, the vertical distance of N and C from the Cu plane are almost identical at 3.35 and 3.32 Å, respectively. On the other hand, empty  $p_z$  states of B localized in the region around the dopant site drive strong interactions with Cu  $d_{z^2}$  and s states (see Supporting Information S2 and Figure S2 and Figure S3). This interaction pulls B closer to the Cu substrate and drives a deformation of the initially flat graphene.<sup>21</sup> In particular, the vertical distances of B and C from the Cu plane are 2.39 and 2.78 Å, respectively. The interaction is observed also from a more apparent charge modulation on top of the Cu surface. This difference between N and B dopant interaction with Cu is found independent of registry to the Cu(111) surface (see Supporting Information S2 for details). Although the B dopant is pulled toward the substrate, we find that the basic shape of the STM image remains the same (Supporting Information S2 and Figure S4), confirming that purely electronic effects

account for the observed differences between graphitic N and B dopants in STM topography.

Interestingly, the differences between the atomic-scale interactions of graphitic B and N dopants have a profound impact on the dopant distribution at larger length scales. In general, graphitic substitution can occur in both graphene sublattices as shown in Figure 2a. In each case, the nearest neighbors of the dopant atom come from the opposing sublattice, resulting in dopant features that have triangular symmetry rotated 180° from one another. STM measurements indicate that the graphitic dopant distribution between the two sublattices is very different in B- and N-doped graphene. Figure 2b,c shows typical  $10 \times 10$  nm<sup>2</sup> areas of B-doped and N-doped graphene films respectively. In these images, the dopants exist in both sublattices and their effects on the image morphology are highlighted (green triangle and red triangle). In the case of B-doped graphene, the dopants are distributed randomly between the two sublattices, while the N-doped graphene shows a strong tendency for the dopants to cluster locally on the same sublattice. This phenomenon is further confirmed in multiple samples and across larger areas, as shown in Figure 2d,e.<sup>12,17,30</sup>

To quantitatively characterize the spatial distribution of the dopants both within and between the sublattices, we analyze statistically the positions of dopants from large area STM images ( $30 \times 30$  nm<sup>2</sup> in Figure 2d,e). We do this by calculating the probability that a given STM image is consistent with a random dopant distribution using two testing methods. In the first test, we simply consider the ratio of the total number of dopants observed in each sublattice for a given image and calculate the likelihood that a random distribution of dopants between two sublattices will result in this ratio. This test can detect sublattice segregation when the size of the STM image is smaller or comparable to the typical domain size of dopants in the same sublattice. For domains smaller than the typical STM image, we use the Moran Index<sup>31</sup> as a test of sublattice

segregation. Both these tests produce p-values<sup>32</sup> which indicate the probability that a given STM images arises from a random distribution of dopants between sublattices (details of how the p-value is calculated for each test is in the Supporting Information S3–S). A p-value greater than 0.05 indicates that the dopant distribution is within two standard deviations of the most probable random distribution.<sup>32</sup> As an example of the application of these tests, consider Figure 2d,e. In the case of the B-doped sample (Figure 2d), the p-value obtained from the ratio test is 0.405 and from the Moran Index test is 0.503. In contrast, the N-doped sample (Figure 2e) results in p-values of  $1.5 \times 10^{-7}$  from the ratio test and  $3.1 \times 10^{-6}$  from the Moran Index test. The tests thus provide additional confirmation for what appears to be evident to the eye from the two figures, B-doped graphene does not show sublattice segregation down to the smallest length scales, whereas N-doped graphene does indeed segregate with domain sizes larger than 30 nm. We investigated multiple B- and N-doped samples using both tests and took the smaller p-value of the two tests to represent the degree of randomness. We plot these values in Figure 2f. We see that the p-values for B dopants for all the images are above 0.1, while those for N dopants are all below  $10^{-6}$ .

To understand this, we need to consider two possible interactions relevant to the phenomenon. First, in the context of doped, free-standing graphene, there exist only small differences between the structures of B–C and N–C bonds. Even though we observe (Figure 1c) significant long-range electronic interactions,<sup>33</sup> they do not affect the total energy significantly at the typical distance of  $\sim 2\text{--}3$  nm between dopants.<sup>34</sup> Second, the B, N, and C atoms are all bound to surface Cu atoms during the growth process, and differences in the B–Cu and N–Cu interaction can cause differences in sublattice segregation.<sup>35,36</sup> Our results shown in Figure 1e,f illustrate that this effect can be quite different between B and N dopants once they are incorporated. While further studies would be required to confirm the exact cause for this behavior, the sublattice correlation we observe in conjunction with different B–Cu versus N–Cu interactions may well reflect the hypothesized role of the metal substrate in the growth process.<sup>37,38</sup> Systematic growth experiments on different substrates can potentially give more insight into this issue. Moreover, our observation of sublattice segregation in N-doped graphene is important for a number of exciting applications. For example, breaking the sublattice symmetry of graphene destroys the pseudospin degeneracy and introduces a band gap at Dirac points. Theoretical work predicts that dopants in the same sublattice are most efficient in breaking the sublattice symmetry.<sup>39</sup> We have not observed such a band gap in our STM spectroscopy experiments thus far (as described below), chiefly because we are studying samples with low dopant concentrations. Future spectroscopy and transport measurements in the heavily doped regime can be employed to elucidate band gap formation.

As discussed earlier, a chief reason to create B-doped graphene is to introduce hole carriers into the graphene sheet, in analogy with the case of electron doping for N-doped graphene.<sup>12,17,29,30</sup> In order to measure the charge carrier density contributed by the graphitic B dopants, we performed detailed STS measurements on B-doped graphene samples. Figure 3a shows two differential conductance ( $dI/dV$ ) spectra taken on (dashed line) and 2 nm away from (solid line) a B dopant. As in the case of N-doped graphene,<sup>12</sup> two depressions are seen in the spectra. The one at the Fermi level (red arrow)

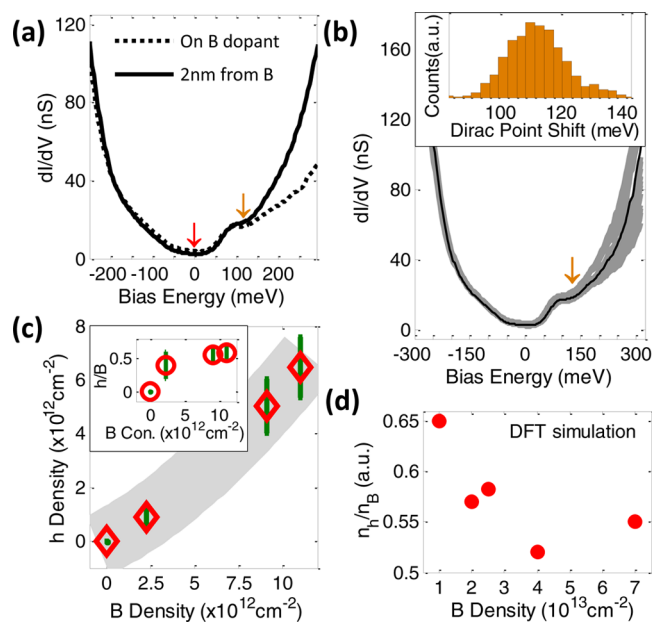


**Figure 3.** (a)  $dI/dV$  spectra taken on (dashed line) and away from (solid line) a B dopant for B-doped graphene on Cu foil with an energy resolution of 10 meV. Red arrow indicates the Fermi level and orange arrow indicates the Dirac point. (b) Spatially averaged  $dI/dV$  spectra (black line) and variations (gray band) over an area of  $30 \times 30 \text{ nm}^2$ . (Inset) Histogram of the spatial variation of Dirac points for B-doped graphene in this  $30 \times 30 \text{ nm}^2$  area.  $V_{\text{bias}} = -0.5 \text{ V}$  and  $I_{\text{set}} = 0.3 \text{ nA}$  (c) Spatially averaged free charge carrier concentration as a function of average boron doping level over four different samples. (Inset) Free charge carrier per B for each of the samples. (d) DFT calculations of free charge carriers per B calculated for five B doping levels.

originates from a phonon-assisted inelastic tunneling process,<sup>40</sup> and the other one (orange arrow) is associated with the Dirac point  $E_D$ .<sup>1</sup> We see that the depression at the Fermi level does not show a well-defined “U” shape that is seen in ref 40, indicating that the direct and phonon-assisted tunneling processes have comparable amplitudes in our measurements. On the basis of the assumption that the ratio of indirect<sup>40</sup> to direct<sup>41</sup> tunneling amplitudes is approximately 1:1, we assign the true Dirac point at the apparent location of the conductance minimum at positive bias minus one-half of the phonon energy (30 meV) with an uncertainty of 30 meV as well. In the particular case of Figure 3a, the conductance minimum is observed at 130 meV giving us a true Dirac point  $E_D$  of  $100 \pm 30 \text{ meV}$ . The Dirac point is located in this sample at positive bias energy, that is, above the Fermi level (orange arrow), indicating that the graphene film is indeed hole doped. The Dirac point position distribution over an area of  $30 \times 30 \text{ nm}^2$  of the film is shown in the inset to Figure 3b. The distribution indicates an average of  $E_D = 110 \pm 32 \text{ meV}$ . Using  $n_h = (E_D^2)/(\pi(\hbar v_F)^2)$  where  $v_F \approx 1.1 \times 10^6 \text{ m/s}$ ,<sup>1,4,5</sup> we estimated a hole concentration of  $n_h = (9.1 \pm 5.5) \times 10^{11} \text{ cm}^{-2}$  in the graphene sheet. By counting the number of B atoms in the measured area, we have a dopant concentration of  $n_B = 2.27 \times 10^{12} \text{ cm}^{-2}$ . The ratio  $n_h/n_B$  gives us the average number of holes contributed per B dopant, which is equal to  $(0.40 \pm 0.24)h/B$  in this area. Detailed STS and STS measurements over multiple B-doped samples with varying B concentration (Figure 3c) show similar doping rates of  $\sim 0.5h/B$ . Our experiment thus indicates that despite structural differences

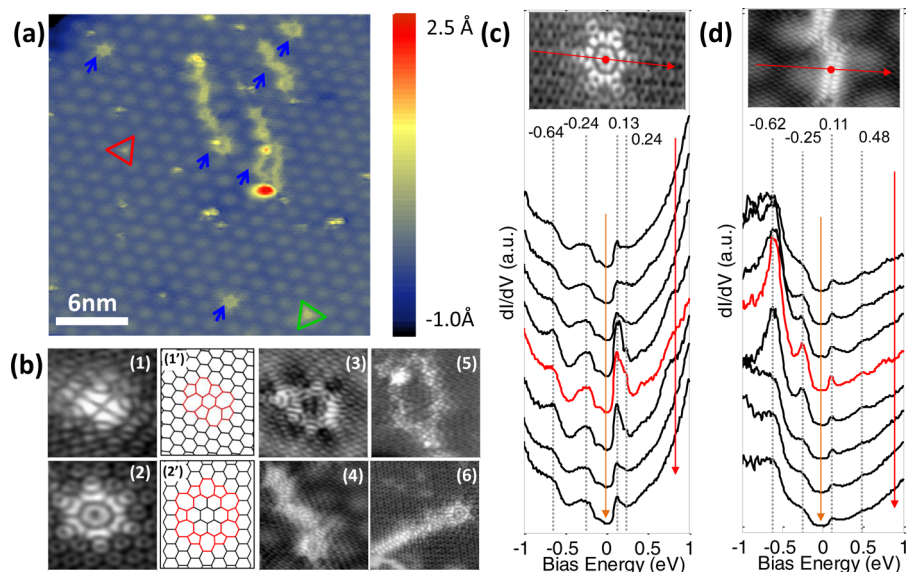


**Figure 4.** (a) STM image of  $30 \times 30 \text{ nm}^2$  area exhibiting multiple defect forms. Red and green triangles indicate the graphitic B dopants in different sublattices. Blue arrows indicate complicated defect forms. (b) STM images of different defect forms associated with pentagon–heptagon pairs. ((1') and (2')) Proposed structures for features in inset (1) and inset (2) respectively.  $V_{\text{bias}} = -0.5 \text{ V}$ ,  $I_{\text{set}} = 0.5 \text{ nA}$ . (c)  $dI/dV$  spectra taken across the features in inset (2) of (c) with the red spectrum taken at the center of the feature.  $V_{\text{bias}} = -0.5 \text{ V}$  and  $I_{\text{set}} = 0.3 \text{ nA}$ . (d)  $dI/dV$  spectra taken across the feature in inset (6) of (c) with red spectrum taken at the center of the feature.  $V_{\text{bias}} = -0.5 \text{ V}$  and  $I_{\text{set}} = 0.3 \text{ nA}$ .

between graphitic N and B doped graphene, the magnitude of the electronic doping caused by the two dopants is very similar. Our DFT calculations of charge density distribution of B- and N-doped graphene (Figure 1e,f, respectively) indicate the charge redistribution extends over several lattice constants from the dopant site. On the whole, DFT calculations show that graphitic B dopants induce a deficiency of charge in the graphene sheet at an average doping rate of  $0.5h/B$  (Figure 3d),<sup>42</sup> consistent with our experimental results.

Thus far, we have studied individual graphitic B dopants, which is the simplest structure produced by  $\text{B}_2\text{H}_6$  addition during CVD growth of graphene. However, we also find that the addition of even small amounts of  $\text{B}_2\text{H}_6$  dramatically enhances the number of topological defects in the graphene film itself during growth. Figure 4a shows a  $30 \times 30 \text{ nm}^2$  scan displaying some of these defect structures (marked by blue arrows), a few graphitic B dopants (marked by red/green triangles), as well as a hexagonal Moire pattern associated with mismatch between graphene and the underlying copper lattice.<sup>43</sup> Close-up images shown in Figure 4b reveal a variety of different topological defects. These include four pentagon–heptagon pairs surrounding a hexagon (inset (1)),<sup>44</sup> a grain boundary loop composed of six pentagon–heptagon rings (inset (2)),<sup>45</sup> and more complicated combinations of pentagon–heptagon defects (inset (3)–(6)). The basic unit of these defect structures is the Stone-Wales (SW) defect that has been observed in graphene prepared by CVD growth on nickel substrates<sup>46,47</sup> and by epitaxial growth on SiC.<sup>45,48</sup> The SW defect is the topological defect with the lowest energy of formation per dislocation.<sup>45</sup> In both pristine graphene and N-doped graphene grown by CVD on copper foil, we do not observe isolated or grouped SW defect structures. The  $\sim 10\%$  concentration of SW defect structures in B-doped graphene is thus related to the presence of B itself during the CVD growth process. Previous experiments on graphite show that the introduction of B atoms into graphite causes interstitial defect loops<sup>49</sup> and introduces roughness in the graphitic basal

plane.<sup>21,22</sup> The similarity of our observation with these previous reports suggests that similar mechanisms are at work in our samples.

Topological defects and grain boundaries are known to produce resonant states near the Dirac point in graphene.<sup>50–52</sup> Their effect on adding or withdrawing charge from the graphene sheet is less well-known. STS measurements of  $dI/dV$  (V) in Figure 4c,d were taken across the features of a “flower” structure (Figure 4b inset (2)) and a “zipper” structure (Figure 4b inset (6)), respectively. The Dirac point  $E_D$  is seen to be close to  $E_F$  for both cases, as indicated by orange arrows. In this area, we also observe almost no graphitic dopants and zero charge carrier doping (see Supporting Information S6 for a  $dI/dV$  spectrum taken far away from the SW defects). This indicates that the SW defect structures do not contribute free charge carriers into graphene. However, the defects introduce resonances in the local DOS at bias voltages of  $\sim -0.6$ ,  $\sim -0.25$ ,  $\sim 0.1$ , and  $\sim 0.25$  eV ( $\sim 0.5$  eV) as shown in  $dI/dV$  spectra in Figure 4c (4d). The resonance energy varies with the geometry of the arrangement of SW defects, varying from  $\sim 0.25$  eV for the flower structure to  $\sim 0.5$  eV for the zipper structure. The width of the regions for the resonance is approximately 5 nm with the maximum intensity observed at the defect sites. The effect of such defects on transport properties depends on the detailed defect structure, and both weak and strong scattering is predicted from different defect configurations.<sup>53,54</sup>

## ASSOCIATED CONTENT

### S Supporting Information

Details of DFT calculations of B/N-doped graphene, calculations of the likelihood of B/N dopants being randomly distributed between the two sublattices of graphene, line profiles of B/N dopants without normalization, and a differential conductance spectrum taken away from SW defects. This material is available free of charge via the Internet at <http://pubs.acs.org>.

## AUTHOR INFORMATION

### Corresponding Author

\*E-mail: pasupathy@phys.columbia.edu.

### Notes

The authors declare no competing financial interest.

## ACKNOWLEDGMENTS

Research supported by the EFRC Center for Re-Defining Photovoltaic Efficiency through Molecule Scale Control (award DE-SC0001085). Support also provided by AFOSR under Grants FA9550-11-1-0010 (A.N.P.), MURI FA955009-1-0705 (G.W.F.), and FA9550-09-1-0691 (J.P.); DOE under Grant DE-FG02-88ER13937 (G.W.F.); NYSTAR and NSF under Grants CHE-07-01483 and CHE-10-12058 (G.W.F.); Samsung Advanced Institute of Technology Global Research Outreach program (J.P.), and the Nano Material Technology Development Program (2012M3A7B4049887) through the National Research Foundation of Korea (J.P.). Portions of this research were carried out at beamlines 11-3 and 13-2 at the Stanford Synchrotron Radiation Laboratory, a national user facility operated by Stanford University on behalf of the U.S. Department of Energy Office of Basic Energy Sciences (DOE-BES), as well as at the Center for Functional Nanomaterials and beamlines X-9 and U7A at the National Synchrotron Light Source, both at Brookhaven National Laboratory and supported by DOE-BES under Contract No. DE-AC02-98CH10886.

## REFERENCES

- (1) Castro Neto, A. H.; Guinea, F.; Peres, N. M. R.; Novoselov, K. S.; Geim, A. K. *Rev. Mod. Phys.* **2009**, *81* (1), 109–162.
- (2) Geim, A. K. *Science* **2009**, *324* (5934), 1530–1534.
- (3) Geim, A. K.; Novoselov, K. S. *Nat. Mater.* **2007**, *6* (3), 183–191.
- (4) Novoselov, K. S.; Geim, A. K.; Morozov, S. V.; Jiang, D.; Katsnelson, M. I.; Grigorieva, I. V.; Dubonos, S. V.; Firsov, A. A. *Nature* **2005**, *438* (7065), 197–200.
- (5) Zhang, Y.; Tan, Y.-W.; Stormer, H. L.; Kim, P. *Nature* **2005**, *438* (7065), 201–204.
- (6) Williams, J. R.; DiCarlo, L.; Marcus, C. M. *Science* **2007**, *317* (5838), 638–641.
- (7) Young, A. F.; Kim, P. *Nat. Phys.* **2009**, *5* (3), 222–226.
- (8) Ashcroft, N.; Mermin, D. *Solid State Physics*; Thomson Learning: Boston, MA, 1976.
- (9) Panchakarla, L. S.; Subrahmanyam, K. S.; Saha, S. K.; Govindaraj, A.; Krishnamurthy, H. R.; Waghmare, U. V.; Rao, C. N. R. *Adv. Mater.* **2009**, *21* (46), 4726–4730.
- (10) Wei, D.; Liu, Y.; Wang, Y.; Zhang, H.; Huang, L.; Yu, G. *Nano Lett.* **2009**, *9* (5), 1752–1758.
- (11) Zhang, C.; Fu, L.; Liu, N.; Liu, M.; Wang, Y.; Liu, Z. *Adv. Mater.* **2011**, *23* (8), 1020–1024.
- (12) Zhao, L.; He, R.; Rim, K. T.; Schiros, T.; Kim, K. S.; Zhou, H.; Gutiérrez, C.; Chockalingam, S. P.; Arguello, C. J.; Pálová, L.; Nordlund, D.; Hybertsen, M. S.; Reichman, D. R.; Heinz, T. F.; Kim, P.; Pinczuk, A.; Flynn, G. W.; Pasupathy, A. N. *Science* **2011**, *333* (6045), 999–1003.
- (13) Sun, Z.; Yan, Z.; Yao, J.; Beitler, E.; Zhu, Y.; Tour, J. M. *Nature* **2010**, *468* (7323), S49–S52.
- (14) Wu, T.; Shen, H.; Sun, L.; Cheng, B.; Liu, B.; Shen, J. *New J. Chem.* **2012**, *36* (6), 1385–1391.
- (15) Wang, X.; Li, X.; Zhang, L.; Yoon, Y.; Weber, P. K.; Wang, H.; Guo, J.; Dai, H. *Science* **2009**, *324* (5928), 768–771.
- (16) Hanafusa, A.; Muramatsu, Y.; Kaburagi, Y.; Yoshida, A.; Hishiyama, Y.; Yang, W.; Denlinger, J. D.; Gullikson, E. M. *J. Appl. Phys.* **2011**, *110* (5), 053504–6.
- (17) Lv, R.; Li, Q.; Botello-Méndez, A. R.; Hayashi, T.; Wang, B.; Berkdemir, A.; Hao, Q.; Elías, A. L.; Cruz-Silva, R.; Gutiérrez, H. R.; Kim, Y. A.; Muramatsu, H.; Zhu, J.; Endo, M.; Terrones, H.; Charlier, J.-C.; Pan, M.; Terrones, M. *Sci. Rep.* **2012**, *2*.
- (18) Zhao, W.; Höfert, O.; Gotterbarm, K.; Zhu, J. F.; Papp, C.; Steinrück, H. P. *J. Phys. Chem. C* **2012**, *116* (8), 5062–5066.
- (19) Wang, H.; Maiyalagan, T.; Wang, X. *ACS Catalysis* **2012**, *2* (5), 781–794.
- (20) Schiros, T.; Nordlund, D.; Pálová, L.; Prezzi, D.; Zhao, L.; Kim, K. S.; Wurstbauer, U.; Gutiérrez, C.; Delongchamp, D.; Jaye, C.; Fischer, D.; Ogasawara, H.; Pettersson, L. G. M.; Reichman, D. R.; Kim, P.; Hybertsen, M. S.; Pasupathy, A. N. *Nano Lett.* **2012**, *12* (8), 4025–4031.
- (21) Endo, M.; Hayashi, T.; Hong, S.-H.; Enoki, T.; Dresselhaus, M. S. *J. Appl. Phys.* **2001**, *90* (11), 5670–5674.
- (22) Kim, E.; Oh, I.; Kwak, J. *Electrochem. Commun.* **2001**, *3* (11), 608–612.
- (23) Kim, K. S.; Zhao, Y.; Jang, H.; Lee, S. Y.; Kim, J. M.; Kim, K. S.; Ahn, J.-H.; Kim, P.; Choi, J.-Y.; Hong, B. H. *Nature* **2009**, *457* (7230), 706–710.
- (24) Li, X.; Cai, W.; An, J.; Kim, S.; Nah, J.; Yang, D.; Piner, R.; Velamakanni, A.; Jung, I.; Tutuc, E.; Banerjee, S. K.; Colombo, L.; Ruoff, R. S. *Science* **2009**, *324* (5932), 1312–1314.
- (25) DFT calculations were performed using the Quantum Espresso package<sup>26</sup> within the local density approximation as parametrized in ref 27. The STM images are simulated using the Tersoff-Hamann approach.<sup>28</sup> Details of the calculations are described in Supporting Information.
- (26) Giannozzi, P.; Baroni, S.; Bonini, N.; Calandra, M.; Car, R.; Cavazzoni, C.; Ceresoli, D.; Chiarotti, G. L.; Cococcioni, M.; Dabo, I.; Corso, A. D.; Gironcoli, S. d.; Fabris, S.; Fratesi, G.; Gebauer, R.; Gerstmann, U.; Gougaudis, C.; Kokalj, A.; Lazzeri, M.; Martin-Samos, L.; Marzari, N.; Mauri, F.; Mazzarello, R.; Paolini, S.; Pasquarello, A.; Paulatto, L.; Sbraccia, C.; Scandolo, S.; Sclauzero, G.; Seitsonen, A. P.; Smogunov, A.; Umari, P.; Wentzcovitch, R. M. *J. Phys.: Condens. Matter* **2009**, *21* (39), 395502.
- (27) Perdew, J. P.; Zunger, A. *Phys. Rev. B* **1981**, *23* (10), 5048–5079.
- (28) Tersoff, J.; Hamann, D. R. *Phys. Rev. B* **1985**, *31* (2), 805–813.
- (29) Zheng, B.; Hermet, P.; Henrard, L. *ACS Nano* **2010**, *4* (7), 4165–4173.
- (30) Joucken, F.; Tison, Y.; Lagoute, J.; Dumont, J.; Cabosart, D.; Zheng, B.; Repain, V.; Chacon, C.; Girard, Y.; Botello-Méndez, A. R.; Rousset, S.; Sporken, R.; Charlier, J.-C.; Henrard, L. *Phys. Rev. B* **2012**, *85* (16), 161408.
- (31) Moran, P. A. P. *Biometrika* **1950**, *37* (1/2), 17–23.
- (32) Lehmann, E. L. *Testing Statistical Hypotheses* (*Springer Texts in Statistics*); Springer: New York, 1997.
- (33) Lambin, P.; Amara, H.; Ducastelle, F.; Henrard, L. *Phys. Rev. B* **2012**, *86* (4), 045448.
- (34) Xiang, H. J.; Huang, B.; Li, Z. Y.; Wei, S. H.; Yang, J. L.; Gong, X. G. *Phys. Rev. X* **2012**, *2* (1), 011003.
- (35) Chakrabarti, D. J.; Laughlin, D. E. *Bull. Alloy Phase Diagrams* **1982**, *3* (1), 45–48.
- (36) Yoshimoto, Y.; Tsuneyuki, S. *Int. J. Quantum Chem.* **2003**, *91* (2), 211–215.
- (37) Artyukhov, V. I.; Liu, Y.; Yakobson, B. I. *Proc. Natl. Acad. Sci. U.S.A.* **2012**, *109* (38), 15136–15140.
- (38) Shu, H.; Chen, X.; Tao, X.; Ding, F. *ACS Nano* **2012**, *6* (4), 3243–3250.
- (39) Rani, P.; Jindal, V. K. arXiv.1209.5228, 2012.
- (40) Zhang, Y.; Brar, V. W.; Wang, F.; Girit, C.; Yayon, Y.; Panlasigui, M.; Zettl, A.; Crommie, M. F. *Nat. Phys.* **2008**, *4* (8), 627–630.
- (41) Xue, J.; Sanchez-Yamagishi, J.; Bulmash, D.; Jacquot, P.; Deshpande, A.; Watanabe, K.; Taniguchi, T.; Jarillo-Herrero, P.; LeRoy, B. J. *Nat. Mater.* **2011**, *10* (4), 282–285.
- (42) Wońska, M.; Miłowska, K. Z.; Majewski, J. A. arXiv.1301.3956, 2012.

- (43) Wintterlin, J.; Bocquet, M. L. *Surf. Sci.* **2009**, *603* (10–12), 1841–1852.
- (44) Cockayne, E. *Phys. Rev. B* **2012**, *85* (12), 125409.
- (45) Cockayne, E.; Rutter, G. M.; Guisinger, N. P.; Crain, J. N.; First, P. N.; Stroscio, J. A. *Phys. Rev. B* **2011**, *83* (19), 195425.
- (46) Park, H. J.; Skákalová, V.; Meyer, J.; Lee, D. S.; Iwasaki, T.; Bumby, C.; Kaiser, U.; Roth, S. *Phys. Status Solidi B* **2010**, *247* (11–12), 2915–2919.
- (47) Meyer, J. C.; Kurasch, S.; Park, H. J.; Skakalova, V.; Künzel, D.; Groß, A.; Chuvalin, A.; Algara-Siller, G.; Roth, S.; Iwasaki, T.; Starke, U.; Smet, J. H.; Kaiser, U. *Nat. Mater.* **2011**, *10* (3), 209–215.
- (48) Guisinger, N. P.; Rutter, G. M.; Crain, J. N.; Heiliger, C.; First, P. N.; Stroscio, J. A. In *Atomic-scale investigation of graphene formation on 6H-SiC(0001)*; AVS: Seattle, Washington, 2008; pp 932–937.
- (49) Turnbull, J. A.; Stagg, M. S.; Eeles, W. T. *Carbon* **1966**, *3* (4), 387–392.
- (50) Peres, N. M. R.; Guinea, F.; Castro Neto, A. H. *Phys. Rev. B* **2006**, *73* (12), 125411.
- (51) Červenka, J.; Flipse, C. F. J. *Phys. Rev. B* **2009**, *79* (19), 195429.
- (52) Yazyev, O. V.; Louie, S. G. *Phys. Rev. B* **2010**, *81* (19), 195420.
- (53) Yazyev, O. V.; Louie, S. G. *Nat. Mater.* **2010**, *9* (10), 806–809.
- (54) Grantab, R.; Shenoy, V. B.; Ruoff, R. S. *Science* **2010**, *330* (6006), 946–948.